Swimming Velocity of Spherical Magnetic Microrobots under Gradient Magnetic Field

Shiqi Ma, Lizhong Xu*

Abstract—**Microrobots have garnered significant attention due to their promising applications in biomedicine. Having a high controllable velocity is one of the goals of realizing efficient and precise targeting applications of microrobots in the future. Compared with the two previous microsphere swimmers, it is found that the swimming velocity of the microsphere changes differently when the driving signal parameters change. Based on this, this paper takes the spherical magnetic microrobot as the research object and carries out experimental research with the gradient magnetic field as the driving source. The changes of magnetic induction strength under different driving signals of hollow coils, iron core coils with iron shells, and coils with special iron core structures are analyzed, respectively. The influence of the change of driving signal on the swimming velocity of the microsphere is analyzed, and the microsphere robot is used to carry out handling experiments on random obstacles. It is found that the magnetic induction intensity generated by different structures of coils under the same driving signal has significantly different rules, which directly leads to significant changes in the swimming velocity of the microsphere. In addition, the viscosity of the liquid environment, the change in the feature size of the microsphere, and the change of the swimming state of the microsphere will also affect the swimming velocity of the microsphere. The handling experiment of the microsphere robot shows that a single microsphere can carry random obstacles, and the multi-microsphere can transform various combination forms under the dynamic gradient magnetic field.**

Index Terms—**driving signal, swimming velocity, gradient magnetic field, microsphere**

I. Introduction

Micro and Nano robots have received increasing attention [1]-[3] due to their significant size advantage for their great potential applications in biomedical fields such as targeted therapies, precise surgical procedures, and medical examinations [4]-[7]. According to the different driving sources, the driving fields of micro and nanorobots can be categorized into electric, thermal, chemical, optical, ultrasonic, and magnetic fields [8]-[11]. Among them, magnetically driven microrobots are widely studied due to their excellent controllability and biocompatibility [12]-[14].

According to the different principles of magnetic drive, magnetic drive mode is mainly divided into rotating magnetic field drive [15], [16], gradient magnetic field drive [17], [18], and oscillating magnetic field drive [19]-[21]. The rotating magnetic field is commonly used to drive microrobots with helical structures [22], [23], which provide good maneuverability and precise motion [24], [25]. However, in order to generate net displacement, the asymmetrical requirements of the microrobot structure increase its manufacturing cost, and the swimming efficiency of the microrobot driven by the rotating magnetic field is only 1% [26]. Similarly, the oscillating magnetic field drive method also requires the design of asymmetric shape deformation to break the “scallop theorem” [27] to produce non-reciprocating motion [28]. Gradient magnetic fields can be generated by position-controlled permanent magnets [29] or magnetic coils [30]-[32]. In contrast, there is no restriction on the structure of the microrobot when driven by a gradient magnetic field, and any structure can produce effective displacement. In addition, in order to reduce surface friction, the microrobot driven by a gradient magnetic field usually adopts a spherical or cylindrical structure [33]-[36].

Swimming velocity is an important index to measure the performance of micro and nanorobots. In addition, for complex working environments, the auxiliary role of algorithms can enhance the control performance [37]-[41]. However, there are few studies on the velocity of micron robots driven by gradient magnetic fields in the current study. Based on this, this paper takes three sets of electromagnetic coils with different structures as the research object and analyzes the changes in magnetic induction intensity generated by them with the driving signal. In addition, the magnetic microsphere is driven by two kinds of iron core coils with different structures, and the changes in the swimming velocity of the microsphere with the driving signal and its parameters are analyzed. Finally, the coil with the largest value of magnetic induction strength under the same signal parameters was selected as the drive source for the drive control experiments of the microrobots. Through comprehensive analysis and in-depth discussion of the changes in magnetic induction intensity of coils with different structures, the relevant characteristics of these coils are identified. Subsequently, by systematically analyzing and discussing the variations in the microsphere swimming velocity when the signals and parameters change, the mechanism of the changes of microsphere swimming velocity under the dynamic gradient magnetic field is revealed. This provides the research basis for the next step to realize the diversified motion control of microrobots under the gradient magnetic field, promoting research progress in this field.

Manuscript received December 27, 2024; revised March 29, 2025.

Shiqi Ma is a PhD candidate of Yanshan University, Qinhuangdao, 066004, China (e-mail: mashiqi@stumail.ysu.edu.cn).

Lizhong Xu is a professor of School of Mechanical Engineering, Yanshan University, Qinhuangdao, 066004, China (corresponding author to provide e-mail: xlz@ysu.edu.cn).

II. MATERIALS AND METHODS

In order to investigate the variation of magnetic induction intensity generated by coils of different structures and the influence on the swimming velocity of microspheres, hollow coils with aluminum alloy as the skeleton, iron core coils wrapped with iron shell, and iron core coils without iron sheet were selected for testing and analysis. In order to simplify the expression, C1, C2, and C3 refer to the hollow coil with aluminum alloy as the skeleton, the iron core coil wrapped in an iron shell and the iron core coil without an iron sheet wrap, respectively. The basic parameters of the three types of coils are shown in Table I and Table II.

TABLE I
ELECTRICAL PARAMETERS OF THE COIL

	Resistance Value (Ω)	Inductance Value(mH)	Capacitance Value(pF)
C1	2.8	1.26	142
C2	254.2	10000	--
C3	3.2	81.46	273.4

TABLE II
ELECTRICAL CHARACTERISTIC PARAMETERS OF THE COIL

	Diameter (mm)	Length (mm)	Zero-Bias Signal Amplitude (V)	Bias Voltage (V)
C1	54	52	1.5	1.5
C2	12	27	1.5	1.5
C3	40	110	1.5	1.5

The materials and equipment used in the experiment are as follows：Magnetic powder (product name, Debai magnetic powder, manufacturer, Shandong Powder Metallurgy Co., LTD.); Glycerol (Glycerol, analytically pure, relative molecular weight 92.09, Tianjin Zhiyuan Chemical Reagent Co., LTD.); Capillary glass tube (Model 3520 rectangular test tube, VitroCom); Power amplifier (Model ATA-304, Xi 'an Antai Electronic Technology Co., LTD.); Signal generator (RIGOL DG1022U); Imaging system (CCD industrial camera, Shanghai Zhiqi Industrial Co., LTD.); Tesla meter (Model HT20, manufactured by Shanghai Hengtong Magneto electric Technology Co., LTD.).

III. MAGNETIC CHARACTERISTICS OF COILS

C1, C2, and C3 were used as research objects to comprehensively analyze the effects of signal and parameter changes on magnetic induction intensity. Zero-bias square wave signal and 1.5V biased square wave signal are precisely applied to the three groups of coils, respectively, and the magnetic induction intensity generated by the three groups of coils is accurately obtained by meticulously changing the frequency of the signals. The results are shown in Fig. 1, where the frequency range of the application is 1 Hz to 100 Hz, and the interval is 5 Hz, aiming to capture detailed variations. In addition, C3 was taken as the research object to specifically analyze the influence of temperature on magnetic induction intensity. The magnetic induction intensity at different temperatures is obtained by conducting rigorous tests at 10 Hz under 1.5V offset square wave signal, and the results are shown in Fig. 1(d). Under the zero-bias square wave signal, the influence of signal duty ratio change on the direction of magnetic induction intensity is not considered, and only the influence of magnetic induction intensity magnitude is considered. When the duty ratio of the signal is changed, the duty ratio change range is 20% to 80% and the interval is 5%. The relationship between the duty ratio and magnetic induction intensity of the three groups of coils at different frequencies is shown in Fig. 2. The maximum frequency is 30 Hz, and the minimum frequency is 1 Hz. Under the 1.5V offset square wave signal, the duty ratio varies from 20% to 80% with an interval of 5%, and the minimum test frequency is 1 Hz and the maximum is 30 Hz. The magnetic induction intensities corresponding to the three groups of coils C1, C2, and C3 under different duty ratios are presented in Fig. 3. Zero-bias square wave signals were applied at 50%, 54%, 58%, 60%, 70%, and 80% duty cycles, respectively, and the magnetic induction intensity generated by the three groups of coils C1, C2, and C3 was obtained by changing the frequency of the signals, as shown in Fig. 4. The results are presented in detail as follows.

A. Study of Magnetic Induction Strength When Considering Temperature Rise

It can be seen from Fig. 1(a) and Fig. 1(b) that under the zero-bias square wave signal and 1.5V offset square wave signal, the magnetic induction intensity generated by C1 and C2 decreases first. Then, with the increase of signal frequency, it becomes stable, and the stable frequency is 10 Hz or above. Among them, under the zero-bias square wave signal, the temperature rise of the C1 coil between 10 Hz and 100 Hz is 16.3℃, and the decrease of magnetic induction intensity is 1 mT. Also under the zero-bias square wave signal, the temperature of the C2 coil rises by 0.4℃ in the frequency range from 10 Hz to 100 Hz, and the magnetic induction intensity shows no decrease (0 mT). Under the 1.5 V offset square wave signal, the magnetic induction intensity of C1 increases by 3 mT when the temperature drops by 29.3℃, and the magnetic induction intensity of C2 fluctuates by 1 mT when the temperature changes by 1.9℃. As can be observed from Fig. 1(c), under the zero-bias square wave signal, the magnetic induction intensity generated by C3 initially decreases and subsequently increases as the drive frequency rises. Likewise, as can be seen from Fig. 1(c), under the 1.5V biased square wave signal, the magnetic induction intensity produced by C3 first decreases and then remains stable as the drive frequency increases. Compared with C1 and C2, the temperature of C3 is constant, and the magnetic induction intensity does not fluctuate during the change of signal frequency. As is illustrated in Fig. 1 (d), with the temperature of C3 rising from 27℃ to 42℃, the magnetic induction intensity generated by the coil drops from 61.4 mT to 59.4 mT. The cumulative decrease during this temperature-increasing process is 2 mT. When a microsphere with a feature size of 15μm is driven, it is found that the magnetic induction intensity that makes the microsphere move is exactly 2 mT. This shows that the influence of the temperature rise caused by coil heating on the magnetic induction intensity value cannot be ignored, so it is necessary to strictly limit the variation range of coil temperature.

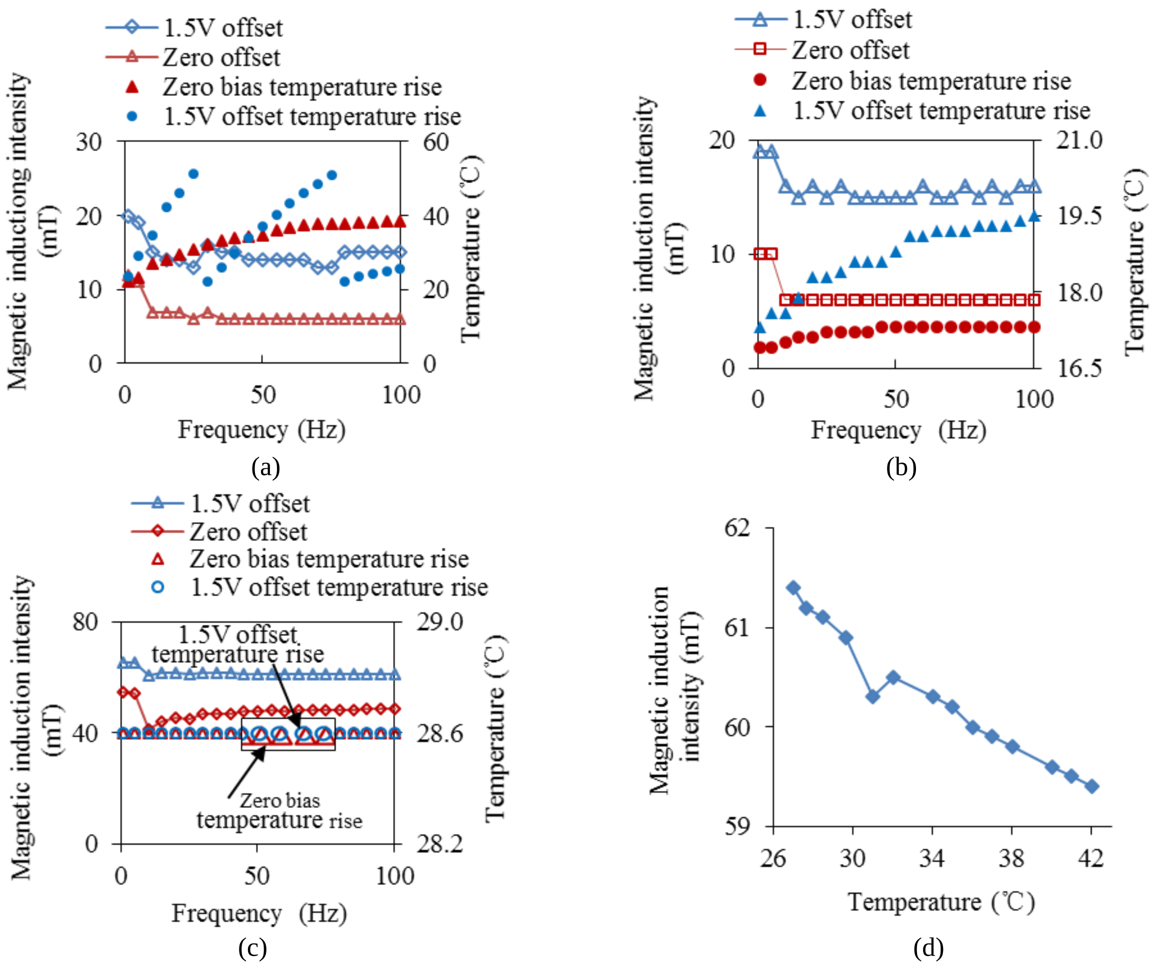

Fig. 1. Relation between magnetic induction intensity and square wave signal frequency under zeros and 1.5V bias ((a), C1; (b), C2; (c), C3; (d), C3).

In addition, comparing Figs. 1(a), 1(b), and 1(c), it is evident that the value of the magnetic induction intensity fluctuates as the temperature of the coil changes. Nevertheless, a small range of temperature fluctuations has no impact on the magnetic induction intensity of C1, C2, and C3 with variations in the signal frequency. This indicates that the coil exhibits a certain degree of tolerance to temperature changes.

By comparing the magnetic induction intensities of C1, C2, and C3, it can be observed that the magnetic induction intensities of C1, C2, and C3 change similarly as the frequency increases under the bias square wave signal. Under the zero-bias square wave signal, as the frequency increases, the magnetic induction intensities of C1 and C2 differ significantly from that of C3. This reveals that when the coil structure and parameters are altered, the influence of frequency on the magnetic induction intensity is mainly manifested in positive and negative alternating signals.

B. Influence of Duty Cycle Ratio on Magnetic Induction Intensity in Zero-Bias Signal

It can be seen from Fig. 2 that under the zero-bias square wave signal, at 1 Hz, the magnetic induction intensities generated by C1, C2, and C3 do not change with the duty ratio. After exceeding 5 Hz, the magnetic induction intensity value is symmetrically distributed with the duty ratio of 50%, which decreases first and then increases with the increase of the duty ratio. At 5 Hz and 10 Hz, the magnetic induction intensity varies significantly with the duty cycle. However, when the frequency surpasses 10 Hz, the magnetic induction intensity varies minimally at the same duty cycle. Further observation reveals that when the frequency exceeds 10 Hz, the magnetic induction intensity generated by C1 and C2 fluctuates erratically as the frequency changes. However, the magnetic induction intensity of C3 exhibits obvious regularity. Specifically, when the duty cycle is close to 50%, the magnetic induction intensity steadily decreases with an increase in frequency; when the duty cycle is substantially less than or substantially greater than 50%, the magnetic induction intensity gradually increases with an increase in frequency, following distinct trends.

A comparative analysis of Figs. 2(a), 2(b), and 2(c) indicates that, at the same frequency, the magnetic induction intensity changes of C1, C2, and C3 follow the same pattern. However, the curves of C1 and C2 fluctuate significantly, while those of C3 are smooth. Furthermore, the variation curves of the magnetic induction intensity of C1, C2, and C3 with respect to the duty ratio at a constant frequency were observed. It is evident that the magnetic induction intensity value on the side where the duty ratio is greater than 50% is slightly smaller than that on the side where the duty ratio is less than 50%. This is mainly attributed to the temperature increase resulting from the coil's long working time. The extended operation time leads to an accumulation of heat in the coil, which in turn affects the magnetic induction intensity.

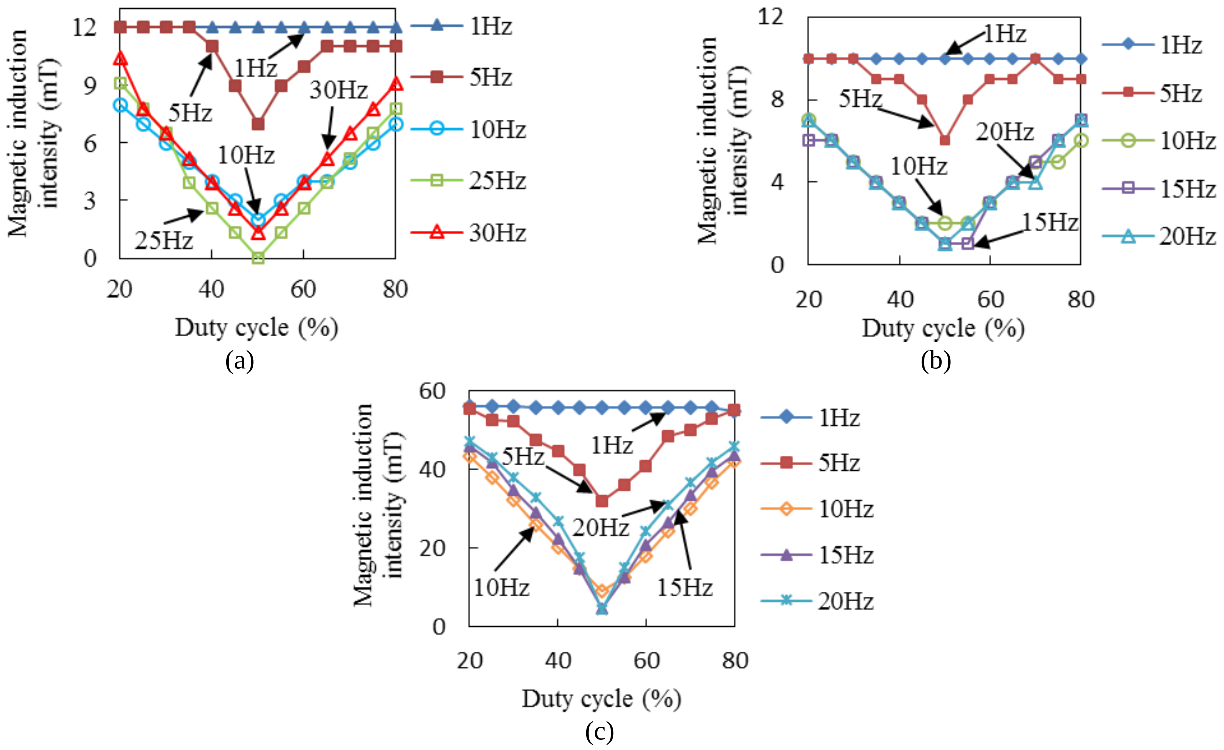

Fig. 2. Relation between magnetic induction intensity and duty cycle under zero-bias square wave signal ((a), C1; (b), C2; (c), C3).

C. Influence of Duty Cycle Ratio on Magnetic Induction Intensity under Biased Signal

It can be seen from Fig. 3 that under the biased square wave signal, the magnetic induction intensity generated by C1, C2, and C3 changes with the duty ratio and frequency in the same way. In particular, the magnetic induction intensity generated by C1, C2, and C3 exhibits distinct variation patterns concerning the duty cycle at different frequencies. Specifically, at 1 Hz, the magnetic induction intensity remains unchanged as the duty-cycle varies. When the frequency is 5 Hz, it initially increases and then stabilizes as the duty-cycle rises. When the frequency exceeds 10 Hz, the magnetic induction intensity demonstrates an upward trend in concert with the increase of the duty cycle. Moreover, this increase in the magnetic induction intensity after the frequency exceeds 10 Hz shows an approximately linear relationship. Further observation reveals that when the duty cycle is set at 70% and the frequency is 5 Hz, the magnetic induction intensity values of C1, C2, and C3 cease to increase with a further increase in the duty cycle. This is because when the duration of the bias square wave signal reaches 0.14 s, the peak magnetic induction intensity can still be detected. This finding indicates that this time length (0.14 s) represents the critical time at which the magnetic induction intensity transitions from an instantaneous value to an effective value.

Combined with Fig. 2 and Fig. 4, it can be found that the magnetic induction intensity generated by C1 and C2 firstly decreases with the increase of frequency at a 50% duty cycle and then tends to zero. When the duty cycle is less than 50%, the magnetic induction intensity decreases first and then stabilizes at a certain value, and the stabilized value increases with the increase of the duty cycle. However, when the duty cycle is 50%, the magnetic induction intensity generated by C3 rapidly decreases with the increase of frequency and then tends to zero. When the duty cycle is near 50% (not exceeding 54%), it first decreases with the increase of frequency and then tends to be stable. When the duty cycle exceeds 56%, it first decreases and then increases with the increase of frequency and then tends to be stable. The minimum value occurs at the signal frequency of 10 Hz.

Additionally, as shown in Fig. 4(d), when the frequency range of the drive signal is further expanded, the following relationship emerges between the duty cycle, signal frequency, and magnetic induction intensity. Regardless of the duty cycle, once the frequency surpasses 100 Hz, wide-ranging changes in the signal frequency will not lead to significant variations in the magnetic induction intensity. This shows that the influence of frequency on magnetic induction intensity only occurs in the low-frequency range from 1 Hz to 100 Hz. A comparison of Figs. 4(a), 4(b), and 4(c) shows that when the duty cycle is no more than 56%, the magnetic induction intensities of C1, C2, and C3 vary with frequency in a similar manner. However, when the duty cycle exceeds 56%, the magnetic induction intensities of C1 and C2 remain constant, and their variation patterns stay unchanged. In contrast, as the frequency increases, the magnetic induction intensity of C3 first decreases, then increases, and finally reaches a stable state. This indicates that the relationship between magnetic induction intensity and frequency is not only associated with the duty cycle but also depends on the coil structure.

In conclusion, when the frequency is below 10 Hz, the magnetic induction intensities of C1, C2, and C3 decrease notably as the signal frequency rises, regardless of whether the signal is a zero-bias square wave or an offset square wave. This observation suggests that the decline in magnetic induction intensity as the signal frequency increases from 1 Hz to 10 Hz is independent of the coil's structure, holding for all three coil configurations.

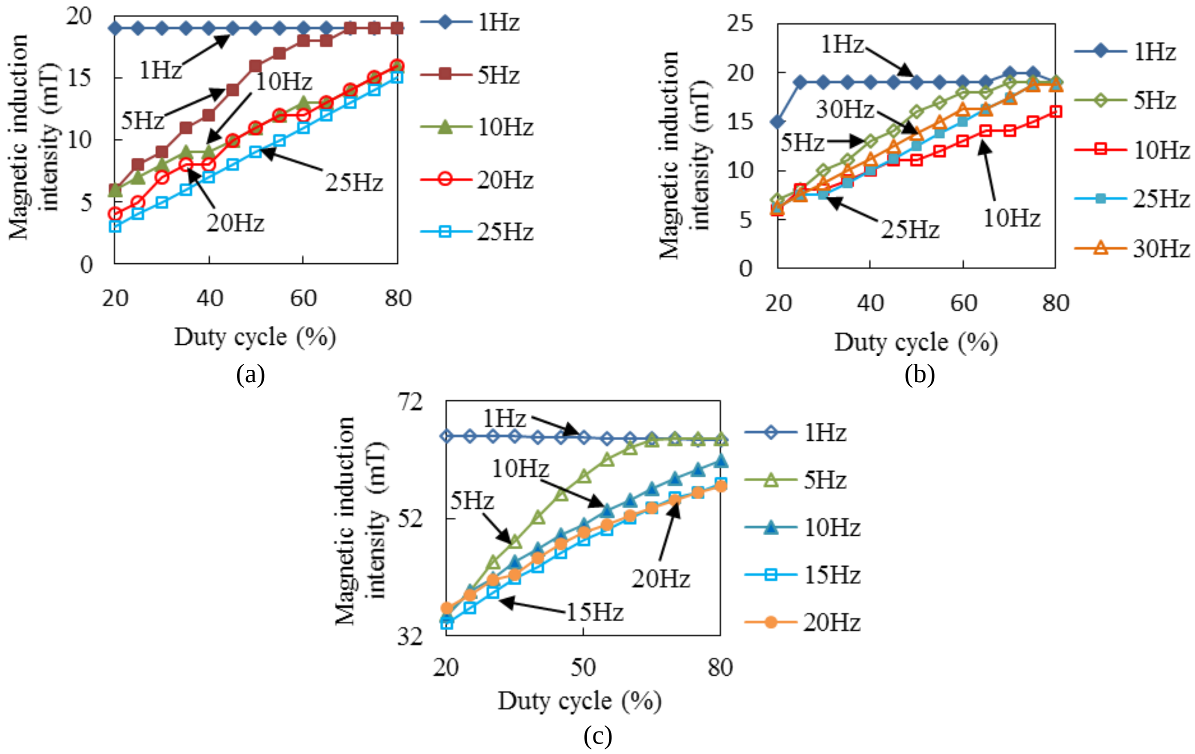

Fig. 3. Relation between duty cycle and magnetic induction intensity under a biased square wave signal ((a), C1; (b), C2; (c), C3).

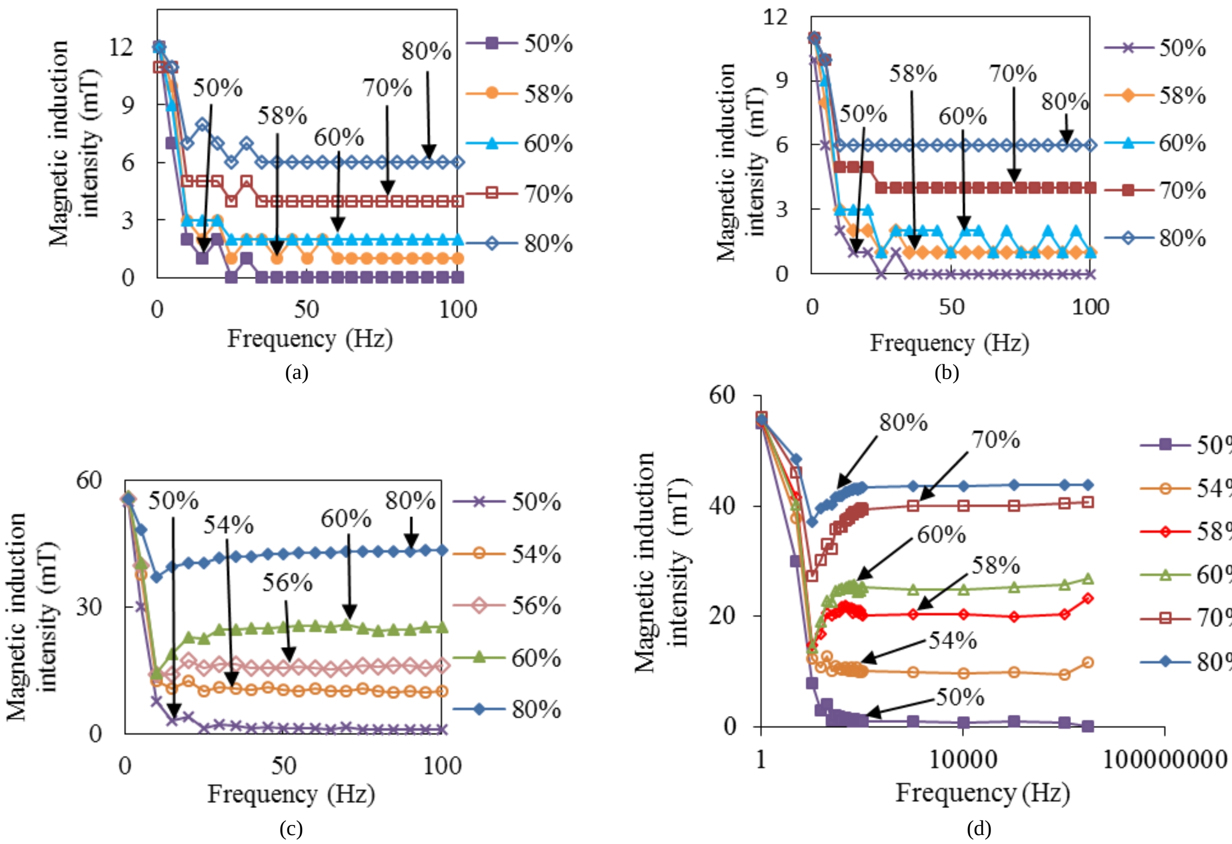

Fig. 4. Relation between frequency and magnetic induction intensity under a biased square wave signal ((a), C1; (b), C2; (c), C3; (d), C3).

Primarily, this is because the frequency changes at a slow pace. The coil can be operated at peak current, so the magnetic induction intensity also reaches its maximum at this time. When the frequency increases, the working current of the coil gradually changes from the peak value to the effective value, so the magnetic induction intensity value decreases rapidly. When the signal frequency reaches 10 Hz or higher, the magnetic induction intensities produced by C1, C2, and C3 under the biased square wave signal are independent of the frequency and solely depend on the signal's duty cycle. These magnetic induction intensities all increase as the duty cycle rises. This is because after the signal frequency increases to 10 Hz, the rise in the duty cycle of the signal is equivalent to increasing the effective current value of the input coil. The increase in effective current will lead to an increase in magnetic induction intensity.

When the signal frequency reaches 10 Hz or higher, the magnetic induction intensity generated by C1, C2, and C3 under the zero-bias square wave signal decreases first and then increases as the duty cycle rises. In this variation process, the magnetic induction intensity reaches its minimum at a 50% duty cycle and exhibits symmetry around this 50% duty cycle. This is primarily attributed to the fact that when the duty cycle is adjusted under the zero-bias signal, the proportion of positive and negative alternating signals within one cycle varies. The magnitude of the effective current that the coil can generate depends on the disparity in the proportion of positive and negative alternating signals. This disparity is defined as “net-output.” Owing to the coil’s inductance, when the net output is zero, the coil exhibits characteristics similar to those of a sinusoidal signal. At that moment, the value of the magnetic induction intensity attains its minimum. When the net output increases, the duty ratio either increases or decreases. This increase in net output is equivalent to increasing the effective current of the system, and thus the magnetic induction intensity value increases.

Under the zero-bias signal, when the signal frequency increases to more than 10 Hz, the magnetic induction intensity generated by C1 and C2 varies with the increase in frequency at different duty cycles. More precisely, it initially decreases and then stabilizes. The magnetic induction intensity produced by C3 is different from that of C1 and C2. When the duty cycle is 50%, as the signal frequency increases, the magnetic induction intensity generated by C3 diminishes. When the duty cycle is 54%, the magnetic induction intensity generated by C3 does not change with the increase of the driving signal frequency. When the duty cycle exceeds 54%, the magnetic induction intensity generated by C3 increases first and then stabilizes with the increase of frequency. This phenomenon is primarily associated with the structural parameters of the coils and the material composition of the iron core. These factors, which render the resistance, capacitance, and inductance values of the coils distinct, also bring about significant differences in the equivalent circuit models of the coils.

IV. Swimming Velocity of Microspheres

C2 was employed as the driving source to measure the swimming velocities of microspheres with characteristic sizes of 21 μm, 39.5 μm, 49 μm, 62.9 μm, 69.9 μm, and 83.9 μm in a glycerol-water mixture, respectively. The outcomes are presented in Fig. 5(a). The proportion of deionized water in the glycerol solution was adjusted to create a fluid environment with varying viscosities. Subsequently, a swimming velocity test was carried out on microspheres with a characteristic size of 21 μm. The results are presented in Fig. 5(b). A sine wave signal, a zero-bias square wave signal, and a biased square wave signal were separately applied to measure the swimming velocity of the microsphere within the frequency range spanning from 1 Hz to 100 Hz. The outcomes of these measurements are presented in Fig. 5(c).

C3 was used as the driving source to test the swimming velocity of a microsphere with a characteristic size of 6.46 μm in a pure glycerol environment. The results of this test are shown in Fig. 6. Among these scenarios, when the signal duty cycle is set at 80% and the frequency ranges from 1 Hz to 3 MHz, the measured swimming velocity of the microsphere is presented in Fig. 6(a) and (b). An offset square wave signal was imposed, and the duty cycle changed from 20% to 80%. The swimming velocity of the microsphere at various frequencies was measured, as depicted in Fig. 6(c). A zero-bias square wave signal was applied. Subsequently, the duty cycle ranged from 20% to 80%, and the swimming velocity of the microsphere at different frequencies was measured, as shown in Fig. 6(d). A sinusoidal signal and a 50% duty cycle zero-bias square wave signal were separately applied to measure the swimming velocity of the microsphere at different frequencies. The results of these measurements are shown in Fig. 6(e). Tests were carried out at 1 Hz, 5 Hz and 10 Hz with 1.5V offset square-wave signals. The swimming velocity of the microsphere at different temperatures was measured, and the results are shown in Fig. 6(f).

A. The Swimming Velocity under C2 Drive

As shown in Fig. 5(a), as the microsphere’s size increases, its swimming velocity rises. This is because a larger size leads to increased magnetization, thus an increased magnetic driving force exerted on the microsphere. As a consequence, the swimming velocity of the microsphere increases. As can be seen from Fig. 5(b), when the viscosity of the liquid increases, the swimming velocity of the microsphere decreases. This is because with the increase in liquid viscosity, the liquid resistance of the microsphere increases while the driving force remains unchanged, so the swimming velocity decreases. As can be observed from Fig. 5(c), under sinusoidal, zero-bias square wave, and biased square wave signals, the microsphere’s moving velocity is associated with the signal frequency. More precisely, the microsphere’s moving velocity declines as the signal frequency rises. This is due to the use of C2 as the driving source. Consequently, the magnetic induction intensities generated by a sinusoidal, a zero-bias square wave, and a biased square wave signal all decline as the signal frequency rises. In turn, the magnetic driving force is reduced, and finally, the swimming velocity of the microsphere is reduced.

However, the velocity curves of the microsphere under zero-bias and biased square-wave signals intersect. This intersection occurs at low signal frequencies, where both polarities of the zero-bias square wave generate an effective driving force. As a result, the influence of coil inductance can be neglected. Unlike the biased square wave, the zero-bias square wave has no zero-signal period. This characteristic leads to a higher microsphere velocity. As the frequency increases under the zero-bias square wave, the coil's inductive reactance rises due to the alternating signal. This causes the driving force generated by the coil to decline rapidly, resulting in a sharp decrease in the microsphere’s velocity. Conversely, under the biased square wave signal, when the frequency increases, the effective driving force generated by the coil does not change significantly. Thus, the velocity of the microsphere decreases but remains higher than that of the microsphere under the zero-bias square wave signal.

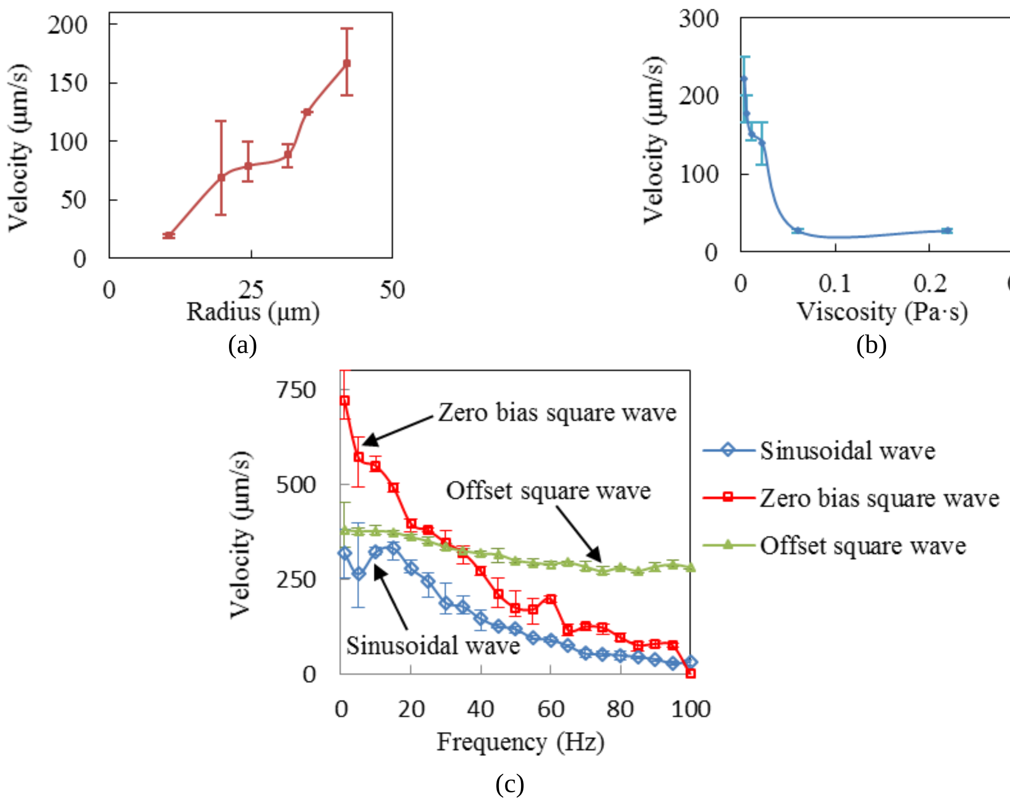

Fig. 5. Change curve of swimming velocity of microsphere driven by C2. (a) The swimming velocity varies with the feature size of the microsphere; (b) The velocity of swimming varies with the viscosity of the liquid; (c) The microsphere velocity varies with the signal frequency.

However, the velocity curve of the microsphere under the zero-bias square wave signal intersects with that under the biased square wave signal. This phenomenon can be ascribed to the situation at low signal frequencies. At low signal frequencies, both the positive and negative components of the zero-bias square wave signal can generate an effective driving force. So the influence of coil inductance can be neglected. In contrast to the biased square wave signal, the zero-bias square wave lacks a zero-signal period throughout the entire signal cycle. As a consequence, the swimming velocity of the microsphere is higher. Under the zero-bias square wave signal, as the frequency further increases, the inductive reactance of the coil increases under the positive-negative alternating signal. This causes the driving force generated by the coil to decline rapidly, resulting in a sharp decrease in the microsphere’s velocity. Conversely, under the biased square wave signal, when the frequency increases, the effective driving force generated by the coil does not change significantly. Thus, the velocity of the microsphere decreases but remains higher than that of the microsphere under the zero-bias square wave signal.

B. Swimming Velocity with C3 Drive

As can be observed from Fig. 6(a), under the zero-bias square wave signal, the swimming velocity of the microsphere varies with frequency. Similarly, the magnetic induction intensity of C3 in Fig. 1(c) varies with frequency. The frequency-dependent variation pattern of the microsphere’s swimming velocity is identical to that of C3’s magnetic induction intensity. This pattern shows that it first declines, then rises, and finally stabilizes. It indicates that the variation in the microsphere’s swimming velocity under a zero-bias square wave signal is predominantly attributed to a particular cause. This cause is the alteration in magnetic induction intensity engendered by the variation in the signal. It can be seen from Fig. 6(b) that under the biased square wave signal, the swimming velocity of the microsphere changes with the increase of the signal frequency. Specifically, the swimming velocity first increases and then becomes stable.

In contrast, the magnetic induction intensity of C3 in Fig. 1(c) first decreases and then gradually becomes stable with the increase of the frequency, showing a different trend from that of the swimming velocity. This is because, under the biased square wave signal, the magnetic induction intensity generated by C3 is alternately changed by “on-off.” When the frequency is low, the microsphere has an obvious pause and a continuous, constant-pressure moving process. When the signal frequency increases, the “on-off” alternating change period of the magnetic induction intensity generated by the coil per unit time increases. During the signal-alternating period, owing to the hysteresis characteristics of C3, the microsphere still undergoes a small displacement at the instant of a signal alternation. Consequently, the microsphere’s moving velocity rises. When the frequency increases to a certain value, the swimming motion of the microsphere under the biased square wave signal is approximately continuous. Therefore, the no-signal period in the “on-off” alternation no longer has a significant influence with the increase of frequency, so the swimming velocity of the microsphere begins to stabilize. In addition, it can be found from Fig. 6 (a) and (b) that there is a specific situation regarding the signal frequency. When the signal frequency exceeds 100 Hz and reaches a maximum of 3 MHz, the swimming velocity of the microsphere remains constant and does not change with the frequency. Furthermore, during the process of frequency variation, the cumulative temperature change of the coil exerts no notable impact on the velocity of the microsphere. This implies that the effect of frequency on the velocity of the microsphere is confined to the low-frequency stage.

It can be seen from Fig. 6(c) that under the conditions of 1 Hz and 5 Hz, the swimming velocity of the microsphere increases steadily with the increase of duty ratio, which is exactly the same as that at 10 Hz and 15 Hz. Nevertheless, at 1 Hz, the magnetic induction intensity generated by C3 remains completely invariant with the increased duty ratio. At 5 Hz, before the duty ratio reaches 65%, the magnetic induction intensity generated by C3 rises gradually with the increase in duty ratio. Once the duty ratio attains 65%, it ceases to vary. This is because, at 1 Hz, the signal varies at a notably slower rate. Even with a 20% duty cycle, the signal duration is able to reach 0.2 s, so the signal is easily detectable. When the frequency rises to 5 Hz, the time of a single signal cycle shortens to 0.2 s. In this case, when the duty cycle is below 65%, the duration of the effective signal is below 0.13 s. Under such circumstances, the magnetic induction intensity varies markedly due to the hysteresis effect of the coil and the hysteresis effect resulting from the duty cycle change. As the duty cycle keeps increasing, the duration of the effective signal grows to over five-fold the time constant, and the impact of the hysteresis effect gradually diminishes. Consequently, the magnetic induction intensity remains unchanged.

As can be observed from Fig. 6(d) and 2(c), under the zero-bias square wave signal, the swimming velocity of the microsphere remains consistently constant with the increase in duty ratio at 1 Hz. Similarly, under the zero-bias square wave signal at 1 Hz, the magnetic induction intensity generated by C3 shows absolutely no variation with the increase in duty ratio. At a frequency of 5 Hz, the magnetic induction intensity first declines and then gradually ascends with an increasing duty ratio. However, the swimming velocity of the microsphere remains invariant with increasing duty ratio. That is because when the signal frequency is low, the positive and negative alternations of the signal are equivalent to the effect of simply two constant-amplitude inverse DC signals.

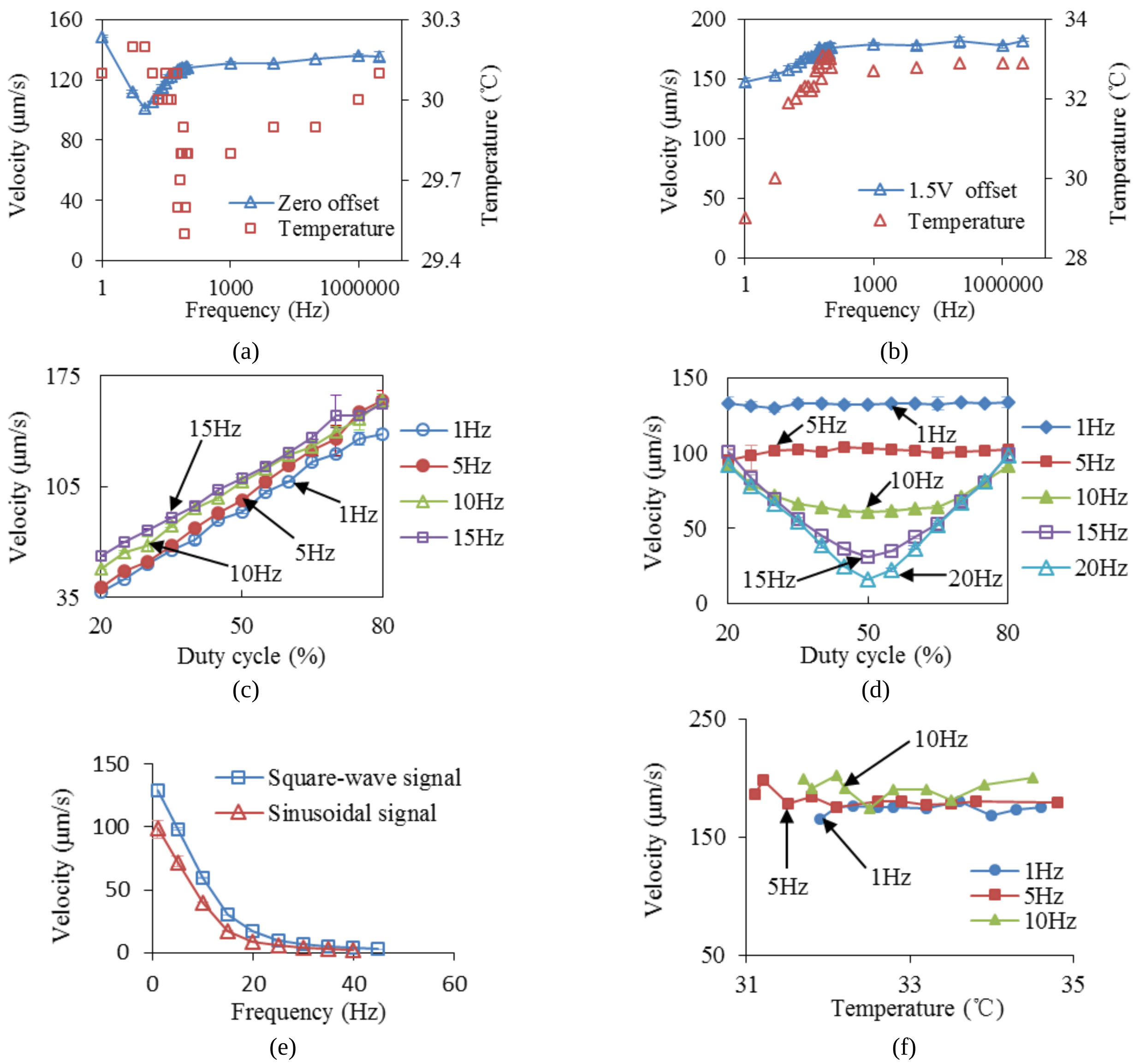

Fig. 6. Change curve of swimming velocity of microspheres driven by C3. (a) The swimming velocity when the frequency changes under zero-bias signal; (b) The swimming velocity when the frequency changes under a 1.5V bias signal; (c) The swimming velocity of 1.5V bias signal varies with the signal duty ratio; (d) Change of swimming velocity with duty ratio under zero-bias signal; (e) The swimming velocity at 50% duty cycle varies with the signal frequency;(f) The variation of swimming velocity when the temperature changes.

Moreover, the ratio of these two signals changes in a predictable pattern. Consequently, the swimming velocity of the microsphere remains unaffected by the duty ratio, maintaining a stable value. When the frequency increases to 5 Hz, the duration of the single-period signal is shortened to 0.2 s. In addition, the magnetic-field-modulation effect caused by signal alternations or reversals starts to influence the amplitude of the magnetic induction intensity, leading to observable fluctuations. However, the alternating magnetic field generated by the signal with polarity reversals serves as an effective driver for the microsphere. Therefore, when the signal’s duty cycle changes, the magnetic induction intensity varies in tandem. Meanwhile, the microsphere velocity continues to be unaffected by the duty ratio, staying consistent. When the signal frequency exceeds 10 Hz, the magnetic induction intensity generated by C3 and the swimming velocity of the microsphere exhibit the same variation pattern when the duty ratio changes. As the duty ratio increases, both initially decline and then ascend in a characteristic pattern.

In addition, in combination with Fig. 6 (e), when a zero-bias square wave signal with a 50% duty cycle is applied, the swimming velocity of the microsphere drops rapidly as the frequency increases. This is the same as that of the variation trend of the swimming velocity as the frequency increases under a sinusoidal signal. Moreover, as the frequency increases, the behavior of the microsphere changes significantly. When the frequency reaches 45 Hz, the microsphere almost no longer swims. This change manifests in two aspects: First, the zero-bias square wave signal at a 50% duty cycle can be approximated to a sinusoidal signal because of their similar harmonic components. Second, the frequency-varying AC characteristic of the zero-bias square wave signal determines the variation law of the microsphere’s motion velocity when the signal changes, affecting its driving efficiency.

It can be seen from Fig. 6(f) that the swimming velocity of the microsphere, under the biased square wave signal, remains relatively stable when the coil temperature increases within the range of 31℃ to 35℃. Moreover, under different temperature conditions, the swimming velocity of microspheres at 10 Hz is greater than that at 5 Hz. Similarly, the velocity at 5 Hz is greater than that at 1 Hz. This shows that variations in a small temperature range do not affect the relationship between the signal frequency and the swimming velocity of the microsphere. Therefore, when the swimming velocity of the microsphere is controlled by adjusting the signal parameters, the coil can withstand a small temperature rise.

Research on coils with different structures shows that under both 1.5V biased and zero-biased square wave signals, adjusting the frequency and duty cycle of the driving signal can alter the coil's magnetic induction intensity. This change in magnetic induction intensity effectively enables adjustment of the microsphere's velocity, providing a reliable means of velocity control. However, at 1 Hz and 5 Hz, when the signal duty cycle changes, the magnetic induction intensity does not correlate with the microsphere's locomotion velocity. Similarly, when the frequency is changed from 1 Hz to 100 Hz at an 80% duty cycle, there is no correspondence between the magnetic induction intensity and the microsphere's swimming velocity. The results demonstrate two key points. First, in the low-frequency stage, changes in magnetic induction intensity with signal parameters do not mirror the variation pattern of the microsphere's swimming velocity. Second, the same situation occurs when the positive-negative signal ratio is large. By comparing C1, C2, and C3, it is evident that when the frequency of the drive signal is adjusted under different duty ratios, the variation patterns of magnetic induction intensity differ substantially. This indicates that changing the coil's structure induces significant alterations in its equivalent circuit model due to differences in the coil's physical parameters.

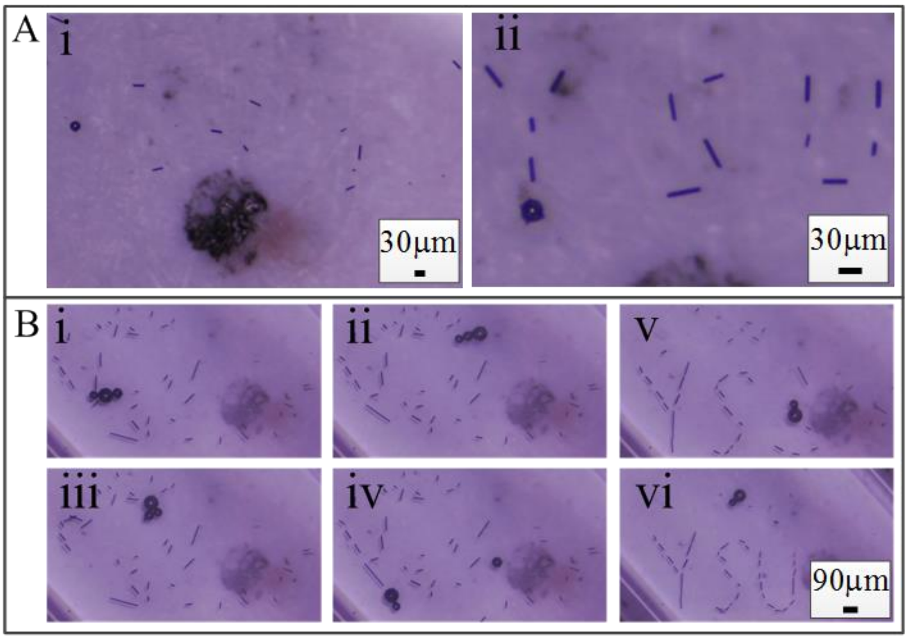

Fig. 7. Motion and control of microspheres. A is the driving experiment of a single microsphere, i is the initial state of a single microsphere, and ii is the letter “YSU” presented by the microsphere pushing the obstacle. B Multi-microsphere control experiment.

V. Motion Control of Microsphere Robot

To validate the actuation performance of the microsphere, a 30 μm diameter microsphere was driven in anhydrous glycerol while a zero-bias square wave signal was applied. The randomly distributed rod-shaped goods were transported, and the three letters “YSU” were eventually placed, as shown in Fig. 7A. Furthermore, to further explore the locomotion characteristics of microspheres under alternating magnetic signals, a cluster of three microspheres was driven to transport randomly distributed cargo. The results are presented in Fig. 7B.

As shown in Fig. 7A, under a zero-bias square wave signal with an 80% duty cycle, the microsphere can move the rod-shaped cargo by “pushing” and “jacking.” When the goods arrive at the designated position, the microsphere propels itself in the opposite direction of the rod-shaped goods to achieve the separation of the microsphere and the goods. Moreover, it achieves the small-angle rotation of the microbar by pushing one end of the rod-shaped goods. The microrod transport experiments show that a single microsphere possesses locomotive and actuation capabilities.

As shown in Fig. 7B, actuated by a zero-bias square wave signal, the three microspheres can assemble into a trimer structure, and their structure simultaneously can be altered by alternating signals. At the initial moment, the three microspheres are coaxial, in a small-large-small arrangement with the big ball in the middle and the small balls on both sides (as shown in Fig. 7B-i). Then, through kinematic transformation, the big ball is relocated to one side, and the three balls still maintain the coaxial, small-small-large arrangement (as shown in Fig. 7B-ii). Subsequently, after further changes, the three spheres are tightly packed in the patterned configuration (as shown in Fig. 7B-iii). In addition, by changing the frequency of the signal, the separation of the microspheres can be achieved, and the trimer structure can be further transformed into a gourd-shaped dimer (as shown in Fig. 7B-iv). As shown in Fig. 7B-v and 7B-vi, in the gourd-shaped form, the dimer microspheres accomplished the transportation of a substantial quantity of random goods and rearranged the three capital letters “YSU.”

VI. Conclusions

In order to explore the key factors affecting the swimming velocity of the microsphere, several experimental analyses were carried out. First, a comparative analysis of the magnetic induction intensity of the three coils C1, C2, and C3 was conducted. Subsequently, the swimming velocity of the microsphere under C2 and C3 was analyzed, and a microsphere driving experiment employing C3 as the driving source was carried out. Through these comprehensive experimental analyses, the following conclusions can be drawn.

1. The coil structures vary. Consequently, their capacitance, inductance, and resistance vary considerably. As a result, the respective equivalent circuit models differ markedly, and the magnetic induction produced by individual coils also varies significantly. At the same time, under the zero-bias square wave signal, when the signal duty cycle is altered, the magnetic induction intensity produced by the coil exhibits substantial variations with the frequency. This is due to the inherent electrical and magnetic properties associated with the coil structure.

3. Under the zero-bias square wave signal, when the signal frequency exceeds 10 Hz, as the duty cycle of the signal is adjusted, the magnetic induction intensity and the swimming velocity of the microsphere vary in accordance with the same pattern. Separately, the swimming velocity of the microsphere reaches a steady-state condition.

4. Under the zero-bias square wave signal, multiple microspheres can aggregate into a polymeric structure via mutual attraction. In the gourd-shaped polymeric structure, modification of the structure and effective goods transportation can be achieved by controlling the alternating signal and the collective action of the microspheres. Moreover, a single microsphere can also transport goods.

References

[1] Marc Z. Miskin, Alejandro J. Cortese, Kyle Dorsey, Edward P. Esposito, Michael F. Reynolds, Qing-Kun Liu, Michael Cao, David A. Muller, Paul L. McEuen, and Itai Cohen, "Electronically Integrated, Mass-Manufactured, Microscopic Robots," Nature, vol. 584, no.7822, pp557-561, 2020

[2] Guang-Zhong Yang, Jim Bellingham, Pierre E. Dupont, Peer Fischer, Luciano Floridi, Robert Full, Neil Jacobstein, Vijay Kumar, Marcia McNutt, Robert Merrifield, Bradley J. Nelson, Brian Scassellati, Mariarosaria Taddeo, Russell Taylor, Manuela Veloso, Zhong-Lin Wang, and Robert Wood, "The Grand Challenges of Science Robotics," Science Robotics, vol. 3, no.14, pp1-14, 2018

[3] Zekui Lyu, Yuning Cao, Michael Yu Wang, and Qingsong Xu, "Concept Design of a Monolithic Compliant Series-Elastic Actuator with Integrated Position and Two-Level Force Sensing," Mechanism and Machine Theory, vol. 193, pp105569, 2024

[4] Xiu Wang, Lijing Qin, Baoqin Song, Mengru Wu, and Wanjun Liang, "Design of A Novel Drug Delivery Nanosystem That Simultaneously Realizes Real-Time Tracing and Drug Delivery Across the Blood-Brain Barrier," Advanced Materials Interfaces, vol. 11, no.6, pp2300738, 2024

[5] Yizong Li, Amro Halwah, Shah R. A. Bhuiyan, and Shanshan Yao, "Bio-Inspired Untethered Robot-Sensor Platform for Minimally Invasive Biomedical Sensing," ACS Applied Materials & Interfaces, vol. 15, no.50, pp58839-58849, 2023

[6] Berta Esteban-Fernandez de Avila, Pavimol Angsantikul, Jinxing Li, Miguel Angel Lopez-Ramirez, Doris E. Ramirez-Herrera, Soracha Thamphiwatana, Chuanrui Chen, Jorge Delezuk, Richard Samakapiruk, Valentin Ramez, Liangfang Zhang, and Joseph Wang, "Micromotor-Enabled Active Drug Delivery for in Vivo Treatment of Stomach Infection," Nature Communications, vol. 8, no.1, pp272, 2017

[7] Carmen Cuntin-Abal, Javier Bujalance-Fernández, Kaisong Yuan, Ana Arribi, Beatriz Jurado-Sánchez, and Alberto Escarpa, "Magnetic Bacteriophage-Engineered Janus Micromotors for Selective Bacteria Capture and Detection," Advanced Functional Materials, vol. 34, no. 16, pp2312257, 2024

[8] Chuanrui Chen, Shichao Ding, and Joseph Wang, "Materials Consideration for The Design, Fabrication and Operation of Microscale Robots," Nature Reviews Materials, vol. 9, no.3, pp159-172, 2024

[9] Manyi Yang, Yaoyu Zhang, Fangzhi Mou, Chuan Cao, Lingxia Yu, Zhi Li, and Jianguo Guan, "Swarming Magnetic Nanorobots Bio-Interfaced by Heparinoid-Polymer Brushes for in Vivo Safe Synergistic Thrombolysis," Advanced Science, vol. 9, no.48, pp1-17, 2023

[10] Xuejiao Zeng, Mingzhu Yang, Hua Liu, Zhenzhong Zhang, Yurong Hu, Jinjin Shi, and Zhi-Hao Wang, "Light-Driven Micro/Nanomotors in Biomedical Applications," Nanoscale, vol. 15, no.46, pp18550-18570, 2023

[11] Fulai Cao, Yanpu Chao, Shuai Lu, Ruirui Guo, and Yaohui Li, "Electric Field-driven Fused Deposition of High-resolution Polycaprolactone Microstructures," Engineering Letters, vol. 32, no.7, pp1385-1393, 2024
[12] Kecheng Quan, Yu Qin, Kai Chen, Miaomiao Liu, Xiaoliang Zhang, Peng Liu, Henny C. van der Mei, Henk J. Busscher, and Zexin Zhang, "Lethal Puncturing of Planktonic Gram-Positive and Gram-Negative Bacteria by Magnetically-Rotated Silica Hexapods," Journal of Colloid and Interface Science, vol. 664, pp275-283, 2024
[13] Yoni Mirzae, Oles Dubrovski, Oded Kenneth, Konstantin I Morozov, and Alexander M. Leshansky, "Geometric Constraints and Optimization in Externally Driven Propulsion," Science Robotics, vol. 3, no.17, pp1-8, 2018
[14] Xinzhao Zhou, Zhekai Ma, Kemin Wang, Guanqing Zhang, Dongni Ren, Wenjun Zhang, Bing Zhang and Ruixue Yin, "Motion Control of Magnetic-Controlled Spiral Microrobots for *In-Vitro* Plaque Removal," IEEE Robotics and Automation Letters, vol. 9, no.6, pp5671-5678, 2024
[15] Wei Zhang, Bin He, Zhen Yin, Chang Xu, Yanmin Zhou, and Yu Cheng, "Autonomous Trajectory Tracking of Bioinspired Soft Microrollers Through a Novel Direction-Speed Decoupled Control Strategy," IEEE Transactions on Automation Science and Engineering, vol. 22, pp3388-3399, 2025
[16] D. von Arx, H. Torlakcik, M. Kim, S. Pane, B. J. Nelson, and Q. Boehler, "Fast Rotating Magnetic Fields in Open Workspace Using Resonant Magnetic Actuation Systems with Magnetic Decoupling," IEEE Robotics and Automation Letters, vol. 9, no.6, pp5276-5283, 2024
[17] Hongzhe Sun, and Shing Shin Cheng, "A Cylindrical Halbach Array Magnetic Actuation System for Longitudinal Robot Actuation Across 2D Workplane," IEEE Robotics and Automation Letters, vol. 9, no.6, pp5847-5754, 2024
[18] Boris Kichatov, Alexey Korshunov, Vladimir Sudakov, Alexandr Golubkov, and Petr Ryapolov, "Droplet Manipulation in Liquid Flow Using of Magnetic Micromotors for Drug Delivery and Microfluidic Systems," Colloids and Surfaces A-Physicochemical and Engineering Aspects, vol. 691, pp133891, 2024
[19] Mohammad Mohaghar, Angelica A. Connor, Shuai Wu, Ruike Renee Zhao, and Donald R. Webster, "Effects of Symmetry-Breaking Mechanisms On the Flow Field Around Magnetic-Responsive Material Appendages That Mimic Swimming Strokes," Physical Review Fluids, vol. 9, no.2, pp023101, 2024
[20] Zhezai Hu, Chengqian Zhang, Haonan Sun, Huangzhe Dai, Daofan Tang, Hao Hu, Tiefeng Li, Jianzhong Fu, Peng Zhao, "A Microstructure Enhancement Method for Hard Magnetic Particle Chains Based On Magnetic Field Oscillation Sieve," Materials & Design, vol. 237, pp112588, 2024
[21] S. Sharanya, Anurag Gupta, and T. Sonamani Singh, "Enhancing Magnetically Driven Microswimmer Velocity Via Low Reynolds Number Hydrodynamic Interactions," Journal of Physics D-Applied Physics, vol. 57, no.15, pp155301, 2024
[22] T Honda, K I Arai, and K Ishiyama, "Micro Swimming Mechanisms Propelled by External Magnetic Fields," IEEE Transactions on Magnetics, vol. 32, no.5, pp5085-5087, 1996
[23] Li Zhang, Jake J. Abbott, Lixin Dong, Bradley E. Kratochvil, Dominik Bell, and Bradley J. Nelson, "Artificial Bacterial Flagella: Fabrication and Magnetic Control," Applied Physics Letters, vol. 94, no.6, pp064107, 2009
[24] Zehao Wu, Yuting Zhang, Ziqiang Chi, and Qingsong Xu, "Design and Development of a New Rotating Electromagnetic Field Generation System for Driving Microrobots," IEEE Transactions on Magnetics, vol. 58, no.1, pp5500108, 2022
[25] Ming Yang, Hanhan Xie, Tiancheng Jiang, Zhen Zhan, Min Ye, Tao Yue, Xiaohui Yan, Xiaopu Wang, and Chengzhi Hu, "MXBOTs: Biodegradable Ti_3C_2 MXene-Based Microrobots for Targeted Delivery and Synergistic Chemo-Photothermal Therapy," ACS Materials Letters, vol. 6, no.5, pp1801-1810, 2024
[26] E. M. purcell, "Life at Low Reynolds Number," American Journal of Physics, vol. 45, no.1, pp3-11, 1977
[27] Xiaohui Yan, Qi Zhou, Jiangfan Yu, Tiantian Xu, Yan Deng, Tao Tang, Qian Feng, Liming Bian, Yan Zhang, Antoine Ferreira, and Li Zhang, "Magnetite Nanostructured Porous Hollow Helical Microswimmers for Targeted Delivery," Advanced Functional Materials, vol. 25, no.33, pp5333-5342, 2015
[28] Tiantian Xu, Zhiming Hao, Chenyang Huang, Jiangfan Yu, Li Zhang, and Xinyu Wu, "Multimodal Locomotion Control of Needle-Like Microrobots Assembled by Ferromagnetic Nanoparticles," IEEE-ASME Transactions on Mechatronics, vol. 27, no.6, pp4327-4338, 2022
[29] Peiran Zhao, Liang Yan, and Xiaoshan Cao, "Magnetic Liquid Metal Droplet Robot with Multifunction and High Output Force in Milli-Newton," Soft Robotics, vol. 10, no.6, pp1146-1158, 2023
[30] Amirhossein Hajiahajani, Dongwook Kim, Ali Abdolali, and Seungyoung Ahn, "Patterned Magnetic Fields for Remote Steering and Wireless Powering to a Swimming Microrobot," IEEE-ASME Transactions on Mechatronics, vol. 25, no.1, pp207-216, 2020
[31] Hui Cao, Liuxi Xing, Jingrong Hu, Hangjie Mo, and Dong Sun, "Automated Control of Microparticle Swarm in A Rotating Gradient-Based Magnetic Field," IEEE Transactions on Automation Science and Engineering, vol. 22, pp2946-2955, 2025
[32] Eric Diller, Joshua Giltinan, Guo Zhan Lum, Zhou Ye, and Metin Sitti, "Six-Degree-of-Freedom Magnetic Actuation for Wireless Microrobotics," International Journal of Robotics Research, vol. 35, no.13, pp114-128, 2016
[33] Shiqi Ma and Lizhong Xu, "Motion Speed Control of Magnetic Microsphere Robot Under Alternating Signals," Sensors and Actuators A-Physical, vol. 378, pp115831, 2024
[34] Hao Qin, Xianyu Peng, Tonghang Sui, Peng Yi, and Jing Li, "Adhesion Performance of Magnetically Responsive Surfaces Under Wet Conditions," Soft Matter, vol. 20, no.8, pp1943-1951, 2024
[35] Angus Unruh, Ethan J. Savage, and Ayusman Sen, "Remote Magnetically Controlled Chemically Fueled Micromotor Disks," Chemistry of Materials, vol. 35, no.23, pp10099-10105, 2023
[36] Jingyu Zhang, Qin Fang, Pingyu Xiang, Rong Xiong, Yue Wang, and Haojian Lu, "Soft Hybrid Actuated Hierarchical Bronchoscope Robot for Deep Lung Examination," IEEE Robotics and Automation Letters, vol. 9, no.1, pp811-818, 2024
[37] Guang Wang, Yanming Zhang, and Qiang Ai, "Lightweight Aerial Target Detection Algorithm with Enhanced Small Target Perception," IAENG International Journal of Computer Science, vol. 51, no.12, pp2123-2134, 2024
[38] Ying Zhang, Guifang Qiao, Di Liu, and Yihan Sun, "Research on a Bionic Ray Robot and its Control Method based on CPG," IAENG International Journal of Applied Mathematics, vol. 55, no.1, pp162-169, 2025
[39] Minoo Jafarlou, Omid Mahdi Ebadati E., and Hassan Naderi, "Improving Fuzzy-Logic based Map-Matching Method with Trajectory Stay-Point Detection," Lecture Notes in Engineering and Computer Science: Proceedings of The International MultiConference of Engineers and Computer Scientists 2023, 5-7 July, 2023, Hong Kong, pp48-57
[40] Sihan Liu, Hailong Yan, Lixia Zhao, and Dongxiang Gao, "Fault Estimate and Reinforcement Learning Based Optimal Output Feedback Control for Single-Link Robot Arm Model," Engineering Letters, vol. 33, no.1, pp21-28, 2025
[41] Linghong Zhu, Xiaochen Huang, Xiaoming Wu, Rui Chen, Dajian Yi, and Wenhui Zhang, "Neural Network Control of Robot under Wheel Slip Conditions based on Observer," Engineering Letters, vol. 32, no.10, pp2041-2051, 2024

Shiqi Ma is a doctoral candidate in machine design and theory at the Yanshan University, China. Her primary research interests are in the area of micro robots and multi-fields coupled dynamics of the micro electromechanical system.

Lizhong Xu received his Ph.D. in machine design and theory from Yanshan University in 1999. He is a professor in machine design and theory at the

Yanshan University, China. His primary research interests are in the area of mechanical transmission, electromagnetic railgun, micro sensors, micro motors and electromechanical integrated system.